Article

In situ valence-transited arsenic nanosheets for multi-modal therapy of colorectal cancer

Hongyue Zheng[1,3] ✉, Ke Zhang[2,3], Jigang Piao[2], Chaofeng Mu[2], Xiaowei Xie[2], Mengying Cheng[2], Tianxiang Yue[2], Jiang Sun[2], Bin Li[2], Yinghui Wei[2], Hangsheng Zheng[2], Lai Jiang[2], Douae Nihed Habiballah[2] & Fanzhu Li[2] ✉

Late-stage and advanced colorectal cancer (CRC) often prove to be resistant to current treatment regimens, due to the evolving tumor microenvironment. Chemotherapy-dominated multi-modal therapeutic strategies based on the specific CRC microenvironment open a new horizon for eradicating colorectal tumors. Here, in situ valence-transited arsenic nanosheets are developed as a multi-modal therapeutic platform by responding to the H_2S-enriched CRC microenvironment. Carrier-free pegylated nanosheets of pentavalent arsenic (As^V), aminooxyacetic acid (AOAA), and copper ion (Cu^{2+}) are innovatively self-assembled via coordination with high loading content and good stability. As^V in pegylated arsenic nanosheets (CAA-PEG NSs) is rapidly released and reduced to trivalent arsenic (As^{III}) to exert its chemotherapy in the local tumor. Furthermore, the immunosuppressive microenvironment is thoroughly remodeled via H_2S depletion of As^V to As^{III} conversion and impairment of H_2S production by AOAA. Additionally, the in situ produced ultrasmall CuS nanoparticles exhibit photothermal activity against CRC under the guidance of photoacoustic imaging. This multi-modal therapeutic strategy, dominated by chemotherapy, completely inhibits CRC progression and prevents its relapse.

Colorectal cancer (CRC) ranks as the third most prevalent cancer and poses a significant threat to human life. The current therapeutic regimens involve the use of chemotherapy, targeted therapy, and radiation therapy, either as a single or combined treatment option for late-stage and advanced metastatic CRC. Despite their use, these regimens are often ineffective, particularly for stage 4 CRC, which presents with a 5-year survival rate of less than 10%[1]. Tumor malignancy is a result of the dynamic changes within the tumor microenvironment, which is composed of various cell types such as vascular cells, cancer-associated fibroblasts, infiltrating immune cells, and other components. These microenvironment factors can positively or negatively influence tumor cell proliferation, energy metabolism, and immune evasion[2]. Multi-modal therapeutic strategies based on the microenvironment-mediated multiple

mechanisms offer new therapeutic avenues that may eradicate colorectal tumors.

Among current treatment regimens, chemotherapy, such as 5-fluorouracil, oxaliplatin, or irinotecan, remains the first-line therapy for advanced CRC[3]. As a potent chemotherapeutic drug, arsenic trioxide has achieved a high complete remission rate of 83–95% in acute promyelocytic leukemia (APL) patients[4]. However, its clinical application in treating solid tumors, including CRC, is limited by its dose-limiting systemic toxicity[5,6]. Previous studies have suggested that both of therapeutic efficacy and systemic toxicity of arsenic compounds depend on their valence state. As^{III}, which has a significantly higher therapeutic potency than As^V, is associated with higher systemic toxicity, while As^V shows the lowest systemic toxicity in vivo[7–9]. Therefore, suppose As^V could be transformed to As^{III} via a reduction

reaction in the local tumor microenvironment; the therapeutic window of arsenic compounds could be significantly enlarged to make arsenic a promising chemotherapeutic agent for solid tumor treatment.

Colorectal cancer is characterized by abnormal upregulation of cystathionine β-synthetase (CBS) and cystathionine γ-lyase (CSE) and their dominant endogenous H_2S production[10–12]. The complex relationship between the endogenous H_2S in the intestinal microenvironment and the high expression of H_2S-producing enzymes in the colorectal cancer microenvironment confers reductive properties on the CRC tumor microenvironment[10,13–15]. This unique reduction microenvironment offers the feasibility to convert As^V to As^{III}. We found that the reduction rate of As^V to As^{III} can reach 67% with H_2S, which is the most robust reductant among the available endogenous reductants in vivo. Furthermore, this reduction reaction process significantly consumes the H_2S content in CRC, partially altering the CRC microenvironment, such as deterring colon cancer cellular bioenergetics and attenuating immunosuppression[16,17].

The therapeutic efficacy of arsenic compounds would be further maximized by making it part of combination therapy. Combination therapy based on the specific CRC microenvironment could be realized via integrating multi-modal therapeutic strategies into one drug delivery system. Even though As^V to As^{III} conversion can consume endogenous H_2S, it is hard to prevent and deplete its production. Aminooxyacetic acid (AOAA) acts as an inhibitor and/or down-regulator of CBS, CSE, and 3-MST, and could inhibit H_2S production effectively, and consequently attenuate colon cancer growth by inducing mitochondrial bioenergetic dysfunction[12,18–20]. On the other

hand, arsenic compound as an inorganic drug has a relatively low loading content and stability in organic nanocarriers, such as liposomes and polymeric nanoparticles[21,22]. As a metalloid, it always forms inorganic complexes as salts or oxides with high arsenic content and stability[23,24]. If arsenic is encapsulated in inorganic functional nanoparticles, it would be an excellent synergistic therapeutic platform for the combination of chemotherapy with other therapies, including immunotherapy, acoustic therapy, photodynamic therapy and photothermal therapy.

In this study, we propose to broaden the potential of arsenic compounds as a non-toxic chemotherapeutic drug via valence-transition for multi-modal combination therapy of CRC based on its unique microenvironment characteristics. Interestingly, we find that As^V, AOAA, and copper ion (Cu^{2+}) can self-assemble into arsenic nanosheets with good stability via molecular dynamics simulation. We further PEGylate the nanosheet, which is stable in blood circulation. Once these pegylated nanosheets are circulated into the H_2S-enriched CRC microenvironment in vivo, they rapidly dissociate into As^V and copper ions, leading to the generation of As^{III} through As^V reduction under H_2S. This mechanism enables As^{III} to exert its chemotherapy effect. Simultaneously, H_2S is depleted via both consumptions of As^V to As^{III} conversion and AOAA-induced enzyme inhibition/downregulation, which remarkably alter the CRC immunosuppressive microenvironment. Furthermore, the locally produced ultrasmall copper sulfide nanoparticles (CuS NPs) with strong NIR-II absorption have photothermal activities against colon cancer under the guidance of photoacoustic imaging. This multi-modal therapeutic approach,
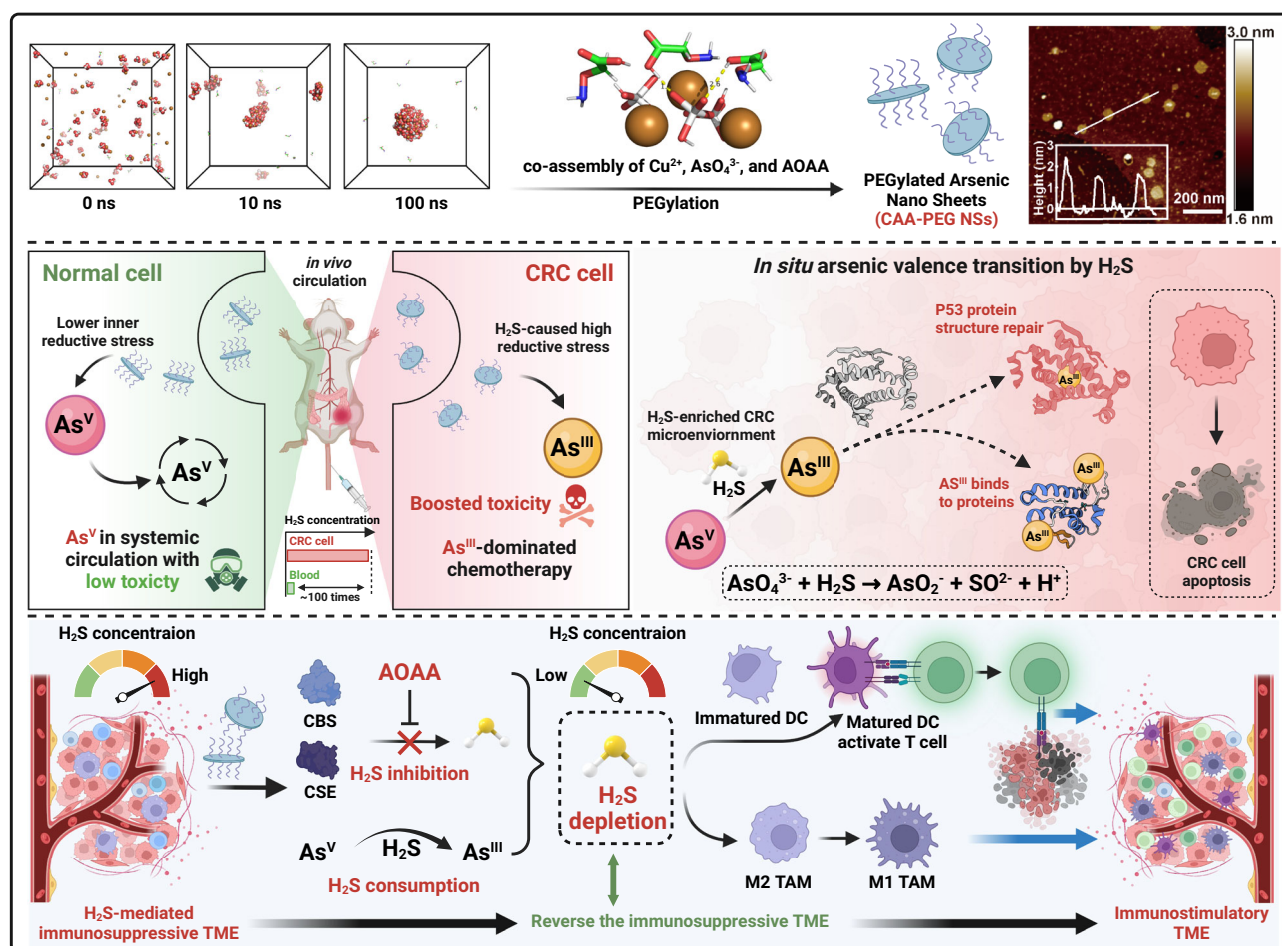

Fig. 1 | The arsenic nanosheets (CAA-PEG NSs) muti-modal treating colorectal cancer via in-situ valence-transit arsenic dominated chemotherapy and H_2S depletion caused immunotherapy. Created in BioRender. *Jiang, L.* (2025) https://BioRender.com/o52q745.

dominated by chemotherapy, inhibits CRC progression and prevents relapses (Fig. 1).

Results

Preparation and characterization of PEGylated arsenic nanosheets

The pegylated arsenic nanosheets (denoted as CAA-PEG NSs) were facilely prepared by copper ions-coordinated multicomponent self-assembly of As^V and AOAA, followed by PEGylation. The morphology of CAA-PEG NSs was observed by transmission electron microscopy (TEM) and atomic force microscopy (AFM) (Fig. 2a, b). The CAA-PEG NSs was ultrathin two-dimensional nanostructure with an average diameter of 100 nm and a thickness of 2 nm. Its zeta potential was reversed to negative (−5.84 mV) after PEGylation (Fig. 2c). The loading content of arsenic, AOAA, and copper in carrier-free CAA-PEG NSs reached 17.5%, 19.2%, and 9.9%, respectively, which is remarkably higher than that in organic nanocarriers such as liposomes and polymeric nanoparticles (Fig. 2d)[25,26]. The arsenic, copper, and oxygen elements distribute homogenously and overlap with each other in elemental mapping images (Fig. 2e), and can be observed by XPS analysis (Fig. S1a).

Molecular dynamics (MD) analysis was conducted to simulate the detailed self-assembly mechanism of CAA NSs (Figs. 2f–i and S2). It was supposed that the self-assembly was mainly driven by Cu^{2+}-dominated multiple driving forces with each other. As can be seen from the simulated trajectory video (Supplementary Movies 1, 2, 3) and key frame conformation, the copper ions and arsenate ions gradually aggregate into stable clusters from an initially random distribution, with these clusters maintaining stability over time (Figs. 2f and S2a, b). Selected from the 20 ns of the interaction conformation of some copper ions and arsenate ions, it can be seen that the copper ions and arsenate ions form a staggered, ordered structure, stabilized by electrostatic interactions (Fig. S2g), leading us to hypothesize that a coordination structure is formed. As a comparison, positively charged sodium ions and negatively charged chloride atoms are not involved in the aggregation (not displayed in the key frames), indicating that the electrostatic interaction between copper ions and arsenate ions is stable (Supplementary Movies 1, 2, 3). From the molecular structure, it is evident that both AOAA and arsenate ions in the system can readily form hydrogen bonds with water. This allows us to further analyze the overall system by examining changes in hydrogen bonding. Analysis of the mutual hydrogen bonding interactions between arsenate ions, AOAA, and H_2O reveals that the number of hydrogen bonds between AOAA and H_2O remains stable (Fig. 2g), while the hydrogen bonds between arsenate ions and H_2O gradually decrease (Fig. 2h). Notably, around 45 ns, the number of hydrogen bonds reaches a near-minimum, indicating that arsenate ions are separating from the H_2O molecules. This separation is also reflected in the RMSD results (Fig. S2c, d). The RMSD analysis indicates the fluctuations of various molecules or ions throughout the simulation process. It shows that as simulation time progresses, the fluctuations of copper ions gradually stabilize (Fig. S2e), suggesting that copper ions have reached a stable state. This stability not only indicates that the simulation system has equilibrated, allowing for subsequent analyses, but also indirectly suggests that the conformation (i.e., a coordination structure) following self-assembly has become stable, leading to an overall equilibrium state in the system. Therefore, by tracking the changes in the RMSD of copper ions, we can gain insight into the movement of copper ions and deepen our understanding of the CAA self-assembly process. Moreover, we observe that arsenate ions and AOAA are also able to produce a small number of hydrogen bonds, a weak interaction between them (Fig. 2i). An analysis of the selected conformation at the 20 ns mark shows that AOAA and arsenate ions can interact through hydrogen bonding (Fig. S2f). Further binding trajectory videos can reveal that AOAA and the arsenate ions can be stably bound for a

limited period, on the order of a few nanoseconds; however, this binding cannot be sustained continuously. We speculate is due to the stronger electrostatic interaction of copper ions with the arsenate ions. Our findings suggest that the coordination between copper ions and arsenate ions, along with the hydrogen bond interaction with AOAA, effectively integrates the individual components into a self-assembled structure.

The physiological stability and dispersibility of pegylated arsenic nanosheets play critical roles in systemic circulation in vivo. CAA-PEG NSs showed negligible agglomeration compared to bare CAA NSs after incubation in PBS for 7 days (Fig. 2j, k). Slight fluctuations in the hydrated particle size, PDI and zeta potential of CAA-PEG NSs were observed in long-term liquid dispersion and stability tests in a simulated blood environment, which demonstrated the excellent stability of CAA-PEG NSs (Fig. S1b–g). All these results suggested that the ultrathin pegylated nanosheets of As^V, AOAA, and Cu^{2+} were successfully self-assembled with high loading content and good stability.

The in vitro performance of PEGylated arsenic nanosheets responded to H_2S

The performance of CAA-PEG NSs responded to the H_2S was investigated. CAA-PEG NSs began to dissociate at 15 min and completely decomposed to ultra-small nanoparticles (about 6 nm) at 120 min in a 3 mM NaHS solution (Fig. 3a). CAA-PEG NSs are pretty stable in pH 7.4 and 6.2 PBS, and there is no arsenic released from nanosheets. However, the arsenic release rate significantly increased with the elevation of NaHS concentration in the release medium. 64% of arsenic was released after 24 h incubation in 3 mM NaHS (Fig. 3b, c). On the other hand, XPS spectrum analysis showed that the reducing ability was proportional to the NaHS concentration. Pentavalent arsenic (As^V) was transformed entirely to trivalent arsenic (As^{III}) in 3 mM NaHS (Figs. 3d, e and S1h, i). These results demonstrated that CAA-PEG NSs were dissociated into As^V rapidly and As^{III} was generated through As^V reduced under a simulated H_2S-enriched microenvironment.

The decomposed ultra-small nanoparticles from CAA-PEG NSs were characterized. The measured lattice spacing of 0.23 nm corresponded well to covellite-phase copper sulfide (105) planes (inner TEM image in Fig. 3a). The selected area electron diffraction (SAED) pattern indicated the polycrystalline structure of the prepared CuS (Inner picture in Fig. 3f). X-ray diffraction (XRD) pattern illustrated that the diffraction peaks correlated with the standard patterns (PDF# 79-2312), indicating that CuS was composed of covellite-phase copper sulfide (Fig. 3f). The ratio of Cu to S was close to 1:1 (Fig. S1j), indicating the formation of CuS nanoparticles. The color of CAA-PEG NSs turned from colorless to brown and black, demonstrating a notable increment in NIR absorbance with a proportional increase at 1064 nm to added NaHS ranging from 0.5 mM to 3 mM (Fig. 3g). Furthermore, the photoacoustic signal of generated ultrasmall CuS nanoparticles at 1064 nm enhanced significantly with increasing NaHS concentrations (Fig. 3h). Thirdly, under 1064 nm NIR irradiation at the power density of 1.0 W/cm² for 5 min, an apparent NaHS concentration-dependent photothermal heating effect was observed (Fig. 3i, j). Meanwhile, they also exhibited excellent photostability with slight maximum temperature variation even after seven cycles of turning the laser on/off process (Fig. 3k). Collectively, pegylated arsenic nanosheets responsively released As^V, and As^V could be reduced to As^{III} in sufficient H_2S sites. The produced ultrasmall CuS nanoparticles had excellent photoacoustic and photothermal capability.

Intracellular behaviors of PEGylated arsenic nanosheets

Here, we further investigated the intracellular behavior of CAA-PEG NSs in colorectal cancer CT-26 cells. CAA-PEG NSs, 2D sheet-like nanomaterials with large surface area and unique surface chemistry, can penetrate cells better than spherical nanoparticles by unique interaction with cells[27–29]. Indocyanine green (ICG)-labeling CAA-PEG
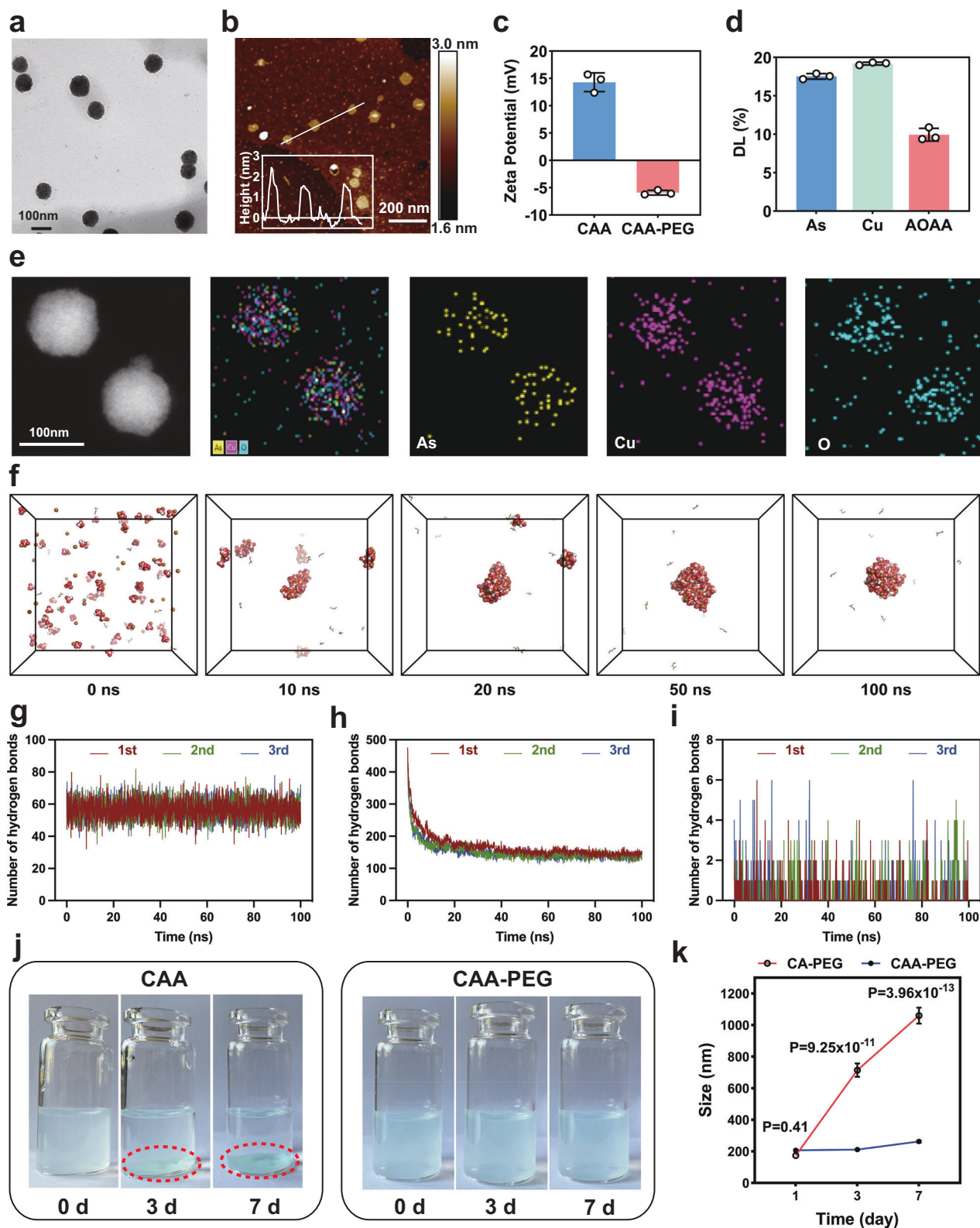
Fig. 2 | Characterization and properties of CAA-PEG NSs. a, b TEM and AFM images of CAA-PEG NSs. **c** The zeta potential of CAA and CAA-PEG NSs (Data are presented as mean values +/− SD, $n = 3$ independent experiments). **d** Loading efficiency of As, Cu, AOAA in CAA-PEG NSs (Data are presented as mean values +/− SD, $n = 3$ independent experiments). **e** Elemental mapping of CAA-PEG NSs. **f** Molecular dynamics simulation of CAA NSs formation process. The hydrogen bonds formed during the CAA NSs formation, AOAA and H_2O (**g**), arsenate ions and H_2O (**h**), and arsenate ions and AOAA (**i**), respectively. The dispersion stability (**j**) and particle size change (**k**) of CAA NSs and CAA-PEG NSs in PBS (Data are presented as mean values +/− SD, $n = 3$ independent experiments. Two-way ANOVA analysis and Sídík's Multiple Comparison Test was used to compare the two groups at the same time point. P values were presented in absolute value in the figures).
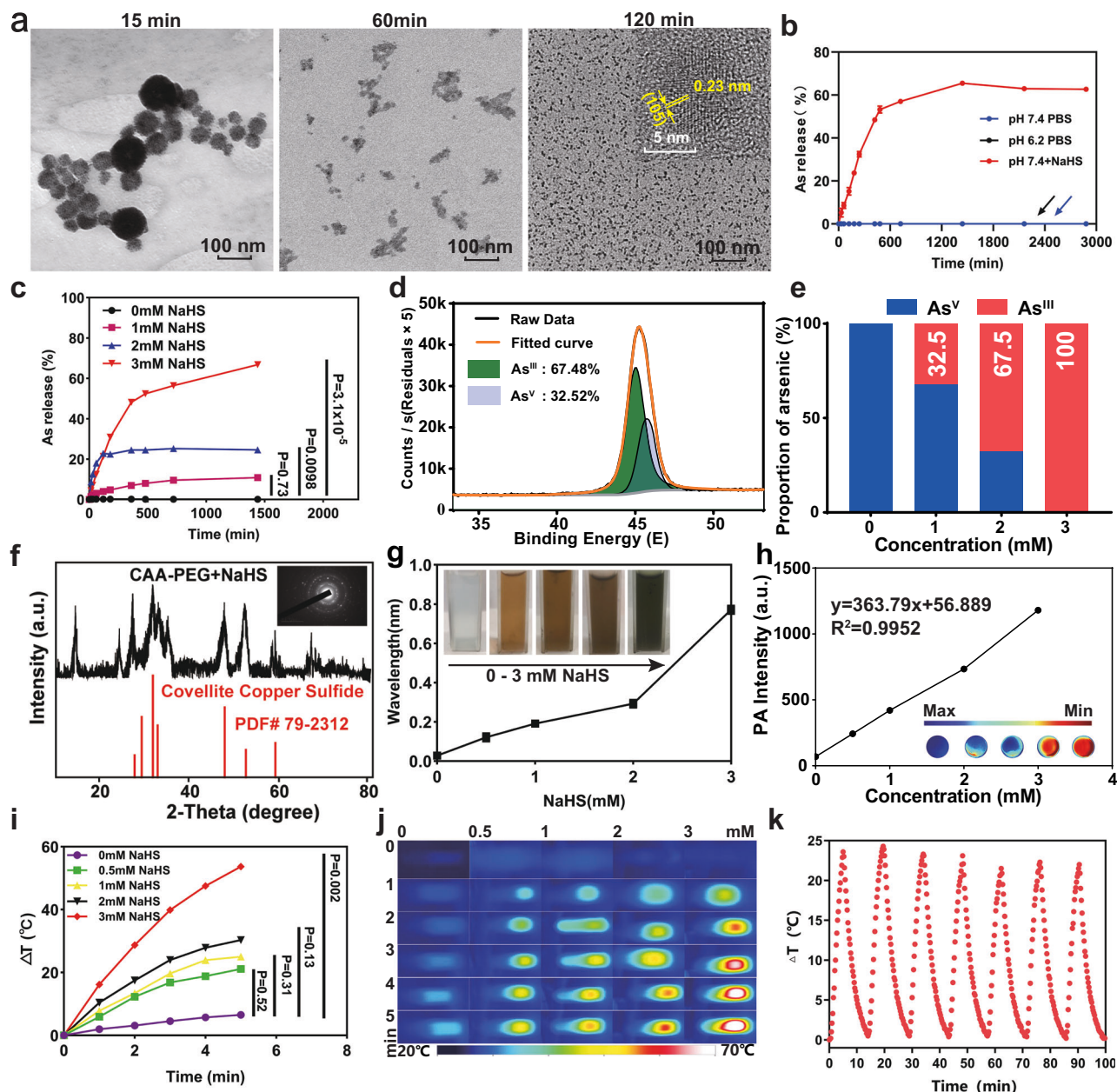
Fig. 3 | H₂S-activated decomposition performances of CAA-PEG NSs in vitro.
a The mimetic H₂S-activated decomposition of CAA-PEG NSs at different time intervals. **b** Arsenic release from different release medium (pH 7.4, pH 6.2, and pH 7.4 + 3 mM NaHS) (Data are presented as mean values +/− SD, $n = 3$ independent experiments). **c** Arsenic release from release medium with escalating NaHS concentrations (Data are presented as mean values +/− SD, $n = 3$ independent experiments). **d** The XPS spectra of As^{III} and As^{V}. **e** Valence transition efficiency of As^{V} to As^{III} of CAA-PEG NSs in different concentrations of NaHS solution. **f** XRD and SAED pattern of ultrasmall CuS nano-particles. **g** UV–vis absorption intensity and color changes (inserted) of CAA-PEG NSs at 1064 nm in different concentrations of NaHS solutions (Data are presented as mean values +/− SD, $n = 3$ independent experiments). **h** Photoacoustic signal intensity of CAA-PEG NSs with various concentrations of NaHS and the corresponding photoacoustic images (inserted) (Data are presented as mean values +/− SD, $n = 3$ independent experiments). The heating curve (**i**) and photothermal images (**j**) of CAA-PEG NSs under 1064 nm laser irradiation with different concentrations of NaHS solution (Data are presented as mean values +/− SD, $n = 3$ independent experiments). **k** Temperature variations of the mixture of aqueous CAA-PEG NSs solutions and NaHS under 1064 nm irradiation for seven light on/off cycles. For (**c, i**) One-way ANOVA with Dunnett's Multiple Comparison Test was used to compare each group with the Control groups. P values were presented in absolute value in the figures.

NSs show much higher cellular uptake (about 3.2 folds) than that of free ICG in CT-26 cells (Fig. 4a). The internalized CAA-PEG NSs rapidly began to degrade within 1 h, almost completely dissociated and formed ultra-small CuS nanoparticles at 6 h (Fig. 4b). Since CBS, CSE and MST were highly expressed in CT-26 cells[12,30], we firstly detected the intracellular H2S concentration in CT-26 cells. It can be seen that the intracellular H2S concentration was up to nearly 40 μmol/L in CT-26 cells, which provided a very favorable condition for arsenic valence transition (Fig. S3a). The experimental results showed that 85% of As^{V}

was transformed into As^{III} in CT-26 cells after cellular uptake of CAA-PEG NSs (Fig. 4c, d). P53 and P21 proteins as apoptosis biomarkers were remarkably upregulated after treatment with CAA-PEG NSs (Figs. 4e and S3b, c).

The intracellular H2S level was examined via fluorescent probe 7-Azido-4-methyl coumarin (AzMC) for its vital role in maintaining the CRC microenvironment[18,31]. Both CA-PEG NSs and CAA-PEG NSs exhibited potent removal effects on intracellular H2S after their internalization in CT-26 cells. The amount of H2S gradually
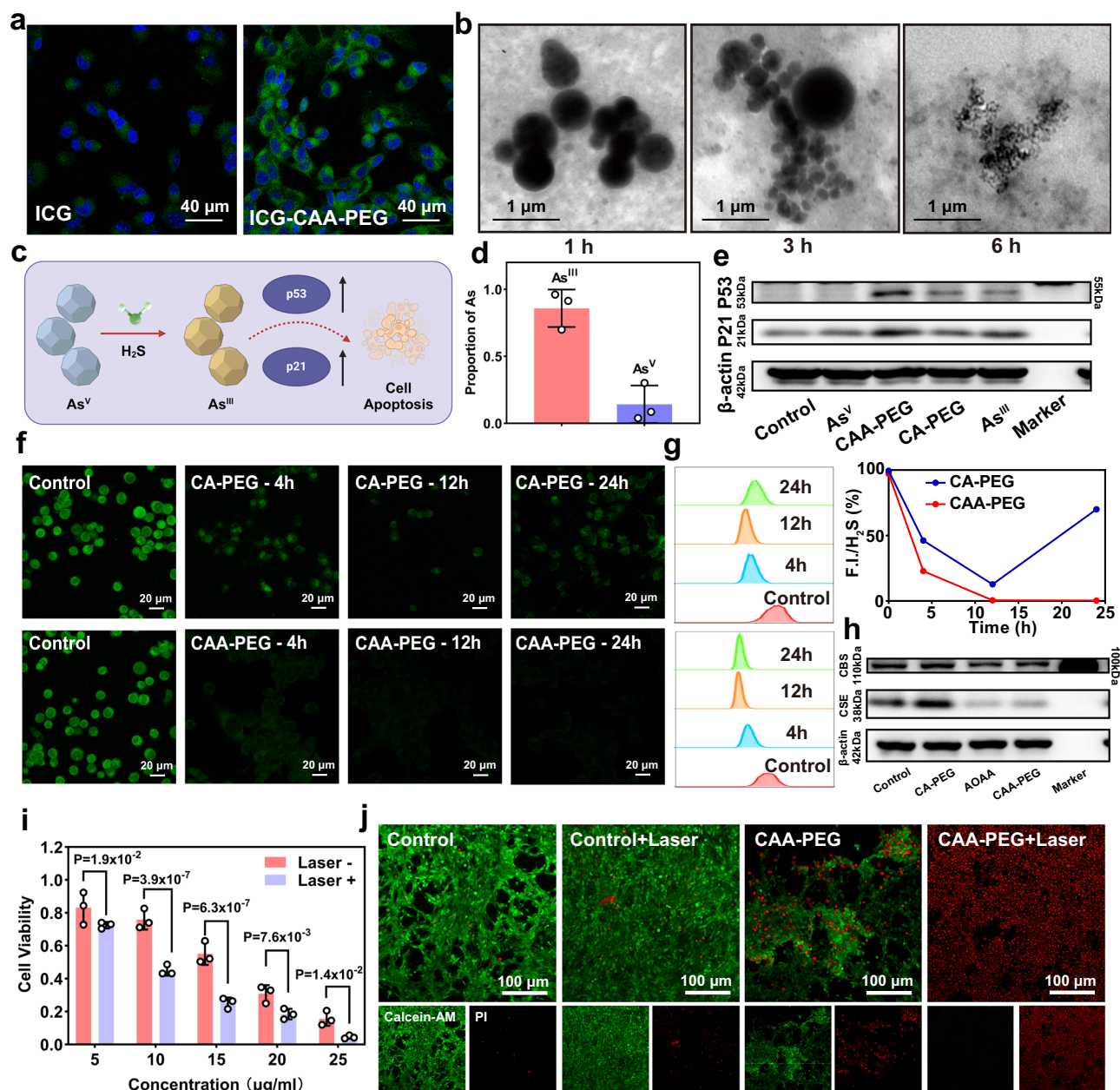
Fig. 4 | Intracellular behaviors of CAA-PEG NSs in colorectal tumor cells.
a Confocal microscopy images of CT-26 cells treated with ICG or ICG-labeling CAA-PEG NSs for 4 h incubation. **b** Bio-TEM images of CT-26 cell sections after incubation with CAA-PEG NSs for different time intervals. **c** Valence transition of As^V to As^{III} of CAA-PEG NSs in CT-26 cells and cell apoptosis causing by As^{III}. Created in BioRender. *Jiang, L.* (2025) https://BioRender.com/b39z422 **d** Valence transition efficiency of As^V to As^{III} in CT-26 cells (Data are presented as mean values +/− SD, $n = 3$ independent experiments). **e** Western blot analysis of cell apoptosis-related proteins (P53, P21) after different treatments (One representative gel from three repeated gels). H_2S content change in CT-26 cells after treatment with CAA-PEG NSs for different time intervals observed by confocal microscopy (**f**) and flow cytometry (**g**), and its quantitation. **h** Western blot analysis of CBS in CT-26 cells after treatment with CAA-PEG NSs (One representative gel from three repeated gels). **i** CT-26 cell viability treated with different concentrations of CAA-PEG NSs with or without laser irradiation (Data are presented as mean values +/− SD, $n = 3$ independent experiments. Two-way ANOVA analysis and Sídík's Multiple Comparison Test was used to compare the Laser +/− groups, *P* values were presented in absolute value in the figures). **j** Live/dead cell staining assay of CT-26 cells after treatment with CAA-PEG NSs with or without laser irradiation.

recovered at 24 h in the CA-PEG NSs group. However, H_2S in the CAA-PEG NSs group was still kept at a low level at 12 h and 24 h (Fig. 4f, g). AOAA as a CBS/CSE/MST inhibitor and CBS/CSE/MST downregulator[32–34] was encapsulated in CAA-PEG NSs, which could downregulate by nearly 40%, 62%, and 37% of CBS, CSE, and 3-MST protein in CT-26 cells, respectively (Figs. 4h and S3d–j), suggesting its considerable inhibition of H_2S production. Similar results were also observed in flow cytometry, which demonstrated that CAA-PEG NSs could deplete H_2S via both consumptions of As^V to As^{III}

conversion and H_2S-relating enzymes inhibition/downregulation of AOAA, thereby reshaping the CRC microenvironment.

CAA-PEG NSs exhibited dose-dependent cytotoxicity on CT-26 cells, which could be further enhanced by laser irradiation at 1064 nm, whereas no apparent cytotoxicity was observed in HepG2 cells (low intracellular H_2S level) (Figs. 4i and S3k, l). Live/dead cell staining shows that around 30% dead cells were observed after incubation with CAA-PEG NSs, and almost all cells are dead by further photothermal effect mediated laser irradiation (Figs. 4j and S4a). Similar results were

also observed by determining CT-26 cell apoptosis (Fig. S4b). Based on our theory and the results of the characterization obtained earlier, we believe that the CAA-PEG NSs decomposed in CT-26 cells at 6 h to form ultra-small CuS nanoparticles and generated a synergistic killing effect based on the photothermal effects generated by their own strong infrared secondary absorption[35]. This property also offers the possibility of multi-modal treatment in mice in vivo.

Arsenic valence transition and the multi-modal combination therapeutic efficacy of PEGylated arsenic nanosheets in vivo

ICG-labelled CAA-PEG NSs were utilized to perform in vivo biodistribution in CT-26 tumor-bearing mice via fluorescence imaging (Fig. 5a). The fluorescence intensity of CAA-PEG NSs at the tumor site after intravenous injection gradually increased and peaked at 12 h, which is much stronger than that of free ICG. It indicates that CAA-PEG NSs increased their circulation time and the distribution in tumors (Fig. 5b, c). The quantitative determination of arsenic concentration by ICP indicated that arsenic was principally distributed in the liver, tumor, and kidney, which was consistent with that detected by in vivo fluorescence imaging (Fig. S3m). On the other hand, the arsenic valence in organs was validated by fluorescence spectrometry. 82.4% of As^V was reduced to As^{III} at the tumor site, followed by 50.4%, 28.4%, 41.7%, and 41.6% in the liver, spleen, lung, and kidney, respectively (Fig. S3n). The results demonstrated that CAA-PEG NSs might reduce the toxic As^{III} in normal tissues.

Photoacoustic imaging (PAI) can be used to determine the tumor location, size, and accumulation of photothermal reagents at the tumor site to achieve photoacoustic diagnosis[36]. The photoacoustic signal monitor shows that the most robust signals were recorded at 8 h post injection, and then gradually declined in the tumor (Fig. 5d). It is probably due to the nanosheet dissociation into ultrasmall CuS nanoparticles in the presence of endogenous H_2S, and eventually cleared from the body. Furthermore, for the photothermal effect investigation, tumor temperature rose to 54.9 °C and 57.9 °C respectively, when exposed to the laser (1.0 W/cm²) for 10 min after intravenous injections of CAA-PEG NSs and CA-PEG NSs (Fig. 5e). These results illustrated that the locally produced ultrasmall CuS nanoparticles with strong NIR-II absorption had excellent photothermal activities under the guidance of photoacoustic imaging.

In vivo anti-tumor capability of CAA-PEG NSs was studied in CT-26 tumor-bearing mice. For each treatment cycle, the mice were injected intravenously with the specified formulations. Two groups received 1064 nm (1.0 W/cm², 10 min) laser irradiation, as depicted in Fig. 5f, and the overall treatment contained three cycles. Compared to CA-PEG NSs alone and CA-PEG NSs+laser groups, the corresponding CAA-PEG NSs and CAA-PEG NSs+laser groups showed superior tumor inhibitory efficacy, which may be owed to the inhibition of H_2S production by AOAA. On the other hand, the tumors were completely eradicated in the CAA-PEG NSs+laser group. The remarkably prolonged survival was achieved in both CA-PEG NSs +laser, and CAA-PEG NSs+laser groups (Fig. 5g). The CAA-PEG NSs +laser group achieved 100% survival on day 90. During the observation period, there were signs of recurrence later in the CA-PEG NSs+laser group. We speculated that the lack of AOAA inhibition of H_2S production following the removal of H_2S is responsible for the tumor recurrence. All mice maintained normal body weight during the treatment period (Fig. S3o). Furthermore, CAA-PEG NSs treated tumors showed significantly increased P53 protein and CBS protein inhibition compared with other groups, confirming their highly effective arsenic-induced tumor cell pro-apoptosis and AOAA-caused H_2S inhibition (Fig. 5h). More importantly, we found from liver and kidney biochemical indices and tissue sections that As^{III} causes irreversible damage to the liver and kidneys, whereas the therapeutic strategy of arsenic valence switching provided by our CAA-PEG NSs was able to significantly reduce these damage states as

well as prevent the emergence of liver and kidney fibrosis compared to As^{III} treatment (Figs. S4c–S6).

In order to provide a more accurate verification of the therapeutic effect of our nano-formulations on colorectal cancer, we established an in-situ model in mice (Fig. S7a). The experimental results showed that, similar to the results in the subcutaneous tumor model, CAA-PEG NSs were able to significantly reduce the size of tumors in mice and significantly elevate the survival rate of mice (Fig. S7b–d). It is worth noting that in the in-situ model, we did not apply laser irradiation, and the above results are only the therapeutic effect of the CAA-PEG NSs itself, which highlights the synergistic therapeutic effect of the integrated application of arsenic valence transition and H_2S inhibitors within the tumor. On the other hand, AOAA inhibits/downregulates H_2S production related enzymes, which may cause associated colonic inflammation[37]. We examined colitis-related indicators in the in-situ mouse model. The results showed that the body weight and colitis-related indicators of the mice were at normal levels for a period of time after treatment with CAA-PEG NSs (Fig. S7e, f). The results of the in-situ model not only illustrate a more comprehensive and realistic picture of the efficacy of our nano-formulations and therapeutic strategies, but also illustrate the safety in a side manner as well (Fig. S7g).

Modulation of CRC immune microenvironment by PEGylated arsenic nanosheet treatment in vivo

PEGylated arsenic nanosheets treatment completely inhibited CRC tumor growth and extended the survival of mice without tumor relapses. Inhibition of endogenous H_2S production has been previously reported to increase the expression of activating/co-stimulatory ligands to reverse the breast tumor immunosuppressive microenvironment[38]. It was speculated that CAA-PEG NSs could modulate CRC immune microenvironment by its H_2S depletion capability in the tumor. Figure 6a shows that CAA-PEG NSs led to dendritic cells (DCs) infiltration in the tumor with consequent activation of T cells to kill tumor cells. A considerable number of mature DCs (32.97%) in tumor-infiltrated lymph nodes were observed in the CAA-PEG NSs treatment group. Mature DCs could further induce T cell-mediated immune response. Compared to the control group, CAA-PEG NSs treatment significantly increased CD8⁺ and CD4⁺ T cell proportions (3.27- and 1.66-fold) in the tumors Fig. 6b, and 3.21-fold and 3.28-fold in the spleen (Fig. S8). The results were also confirmed by immuno-fluorescence analysis of CD8⁺ T cells (Fig. S9a). Moreover, the increased cytokine secretions of interferon-γ (IFN-γ), tumor necrosis factor-α (TNF-α), and interleukin-1β (IL-1β) in the serum could be further anticipated to improve the anti-tumor immune response (Fig. 6c–e). These results implied that CAA-PEG NSs could inhibit tumor growth by promoting DC cell maturation and induction of T cell differentiation.

We further analyzed the tumor-associated macrophages (TAMs) in the tumor after treatment for that TAMs play a crucial role in CRC as abundant and active infiltrated inflammatory cells. A remarkable increase of M1 TAMs and a decrease of M2 TAMs were observed in the tumor following CAA-PEG NSs treatment (Fig. 6f, g). Furthermore, M1 macrophage (CD86) in tumor tissue by immunofluorescence staining also substantiated this phenomenon (Fig. 6h). On the other hand, the detected interleukin 6 (IL-6, secreted by M1 TAMs) and interleukin 10 (IL-10, secreted by M2 TAMs) level changes in serum further verified the increased ratio of M1 to M2 TAMs (Fig. 6i). These results indicated that CAA-PEG NSs could reverse the immunosuppressive microenvironment by re-polarizing M2 TAMs to M1 TAMs.

Mechanisms of PEGylated arsenic nanosheet-mediated anti-tumor immunotherapy

To explore the mechanism of CAA-PEG NSs-mediated anti-tumor immunotherapy, proteomic analysis was performed on control and CAA-PEG NSs treatment groups. Proteomics analysis can characterize
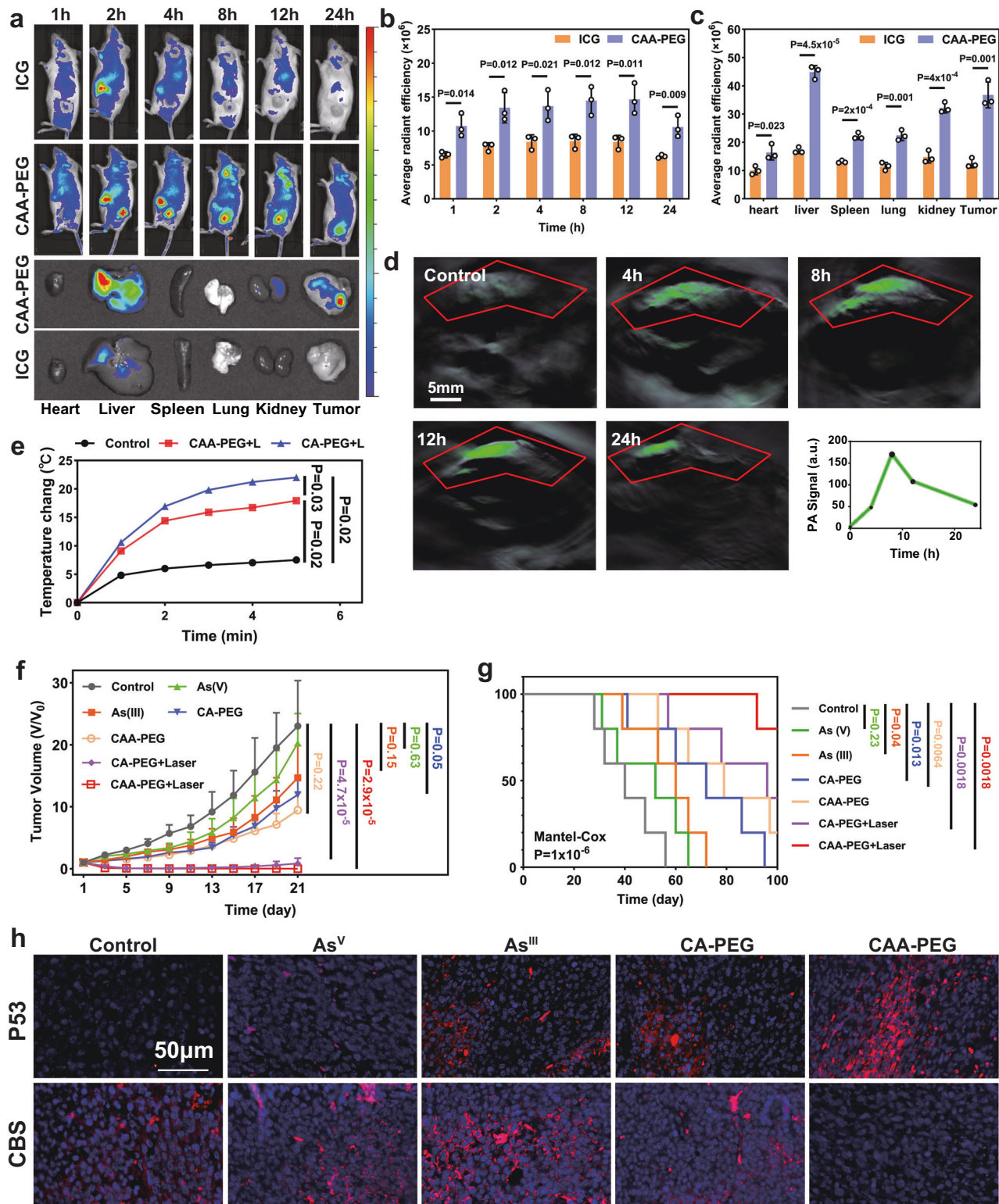
Fig. 5 | In vivo behaviors of CAA-PEG NSs and its multi-modal therapeutic efficacy for CRC treatment. Free ICG or ICG-labelled CAA-PEG NSs -mediated fluorescence distribution in CT-26 tumor-bearing mice and main organs (**a**) and their semi-quantitative analysis (**b**, **c**) (Data are presented as mean values +/− SD, $n = 3$ mice. Unpaired t-tests for each comparison were used. P values were presented in absolute value in the figures). **d** Photoacoustic images of CT-26 tumor-bearing mice before (control) and after intravenous injection of CAA-PEG NSs at 4, 8, 12, and 24 h. **e** Tumor temperature changes after 8 h intravenous injection of CAA-PEG NSs and then upon laser irradiation for 10 min. Data are presented as mean values +/− SD, $n = 3$ mice. One-way ANOVA with Tukey's Multiple Comparison Test was used to compare the mean of each group with the mean of each other groups. P values were presented in absolute value in the figures. Tumor size (**f**), survival curve (**g**) and body weight (Fig. S3o) of CT-26 tumor-bearing mice after various treatments (Data are presented as mean values +/− SD, $n = 5$ mice. For (**f**) One-way ANOVA with Dunnett's Multiple Comparison Test was used to compare each group with the Control groups. P values were presented in absolute value in the figures. Significant differences in survival (**g**) were calculated by the Mantel−Cox test and P values were presented in absolute value in the figure). **h** Immunofluorescent staining assays (P53 and CBS) were performed on tumor sections after different drug treatments.
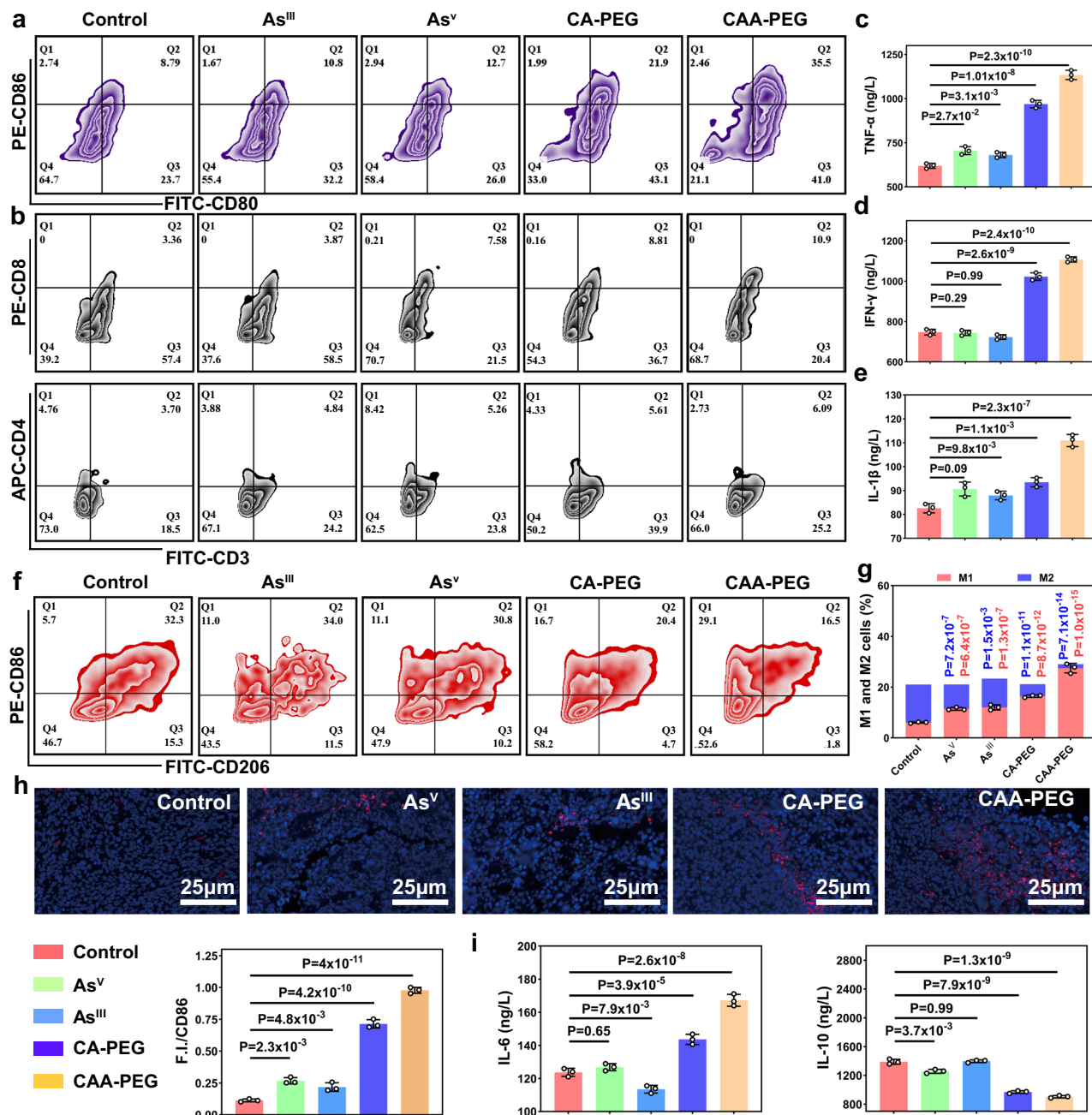
Fig. 6 | Alteration in CRC immune microenvironment after CAA-PEG NSs treatment in vivo. a The percentages of DC maturation in tumors following different treatments (gated on CD11c^{+} DC cells). **b** The percentages of tumoral CD4^{+} and CD8^{+} T cells following various treatments (gated on CD3^{+} T cells). The cytokines secretion of TNF-α (**c**) IFN-γ (**d**) and IL-1β (**e**) in serum following various treatments. The percentages (**f**) and statistical analysis (**g**) of M1 and M2 TAMs after different treatments (gated on F4/80 macrophages). **h** Immunofluorescent staining

(M1-CD86) of tumor sections after different treatment. **i** The cytokine secretion of IL-6 and IL-10 in serum following different treatments. The gating strategy is presented in Fig. S10. For all figures here, data are presented as mean values +/− SD, $n = 3$ mice. One-way ANOVA with Tukey's Multiple Comparison Test was used to compare the mean of each group with the mean of the Control group. P values were presented in absolute value in the figures.

the pathophysiological alternations in diseased tissues. A total of 6968 quantifiable proteins have been detected. On the basis of these quantifiable proteins, we highlighted any differences or similarities between tumor samples by principal component analysis (PCA) (Fig. S9b), where evident separations between control and CAA-PEG NSs group were observed, demonstrating the dynamic alternation of protein expression induced by CAA-PEG NSs treatment. After further normalization, 374 differentially expressed proteins were detected (Figs. 7a and S9c). Of these proteins, 191 were upregulated, and 183 were downregulated ($P < 0.05$) (Fig. 7b, c).

In order to understand how CAA-PEG NSs reshape the tumor immune microenvironment, we further screened immune-related differential expressed proteins. We found that 43 proteins were involved, of which 7 were downregulated and 36 were upregulated. The heat map of differential proteins is shown in Fig. 7d. Pathway analysis based on Gene Ontology (GO) process demonstrated that these 43 differentially expressed proteins enriched significantly in immune processes, particularly involved in humoral immune response, lymphocyte-mediated immunity, T cell-mediated immunity, cell killing, reactive oxygen species metabolic process. (Fig. 7e),
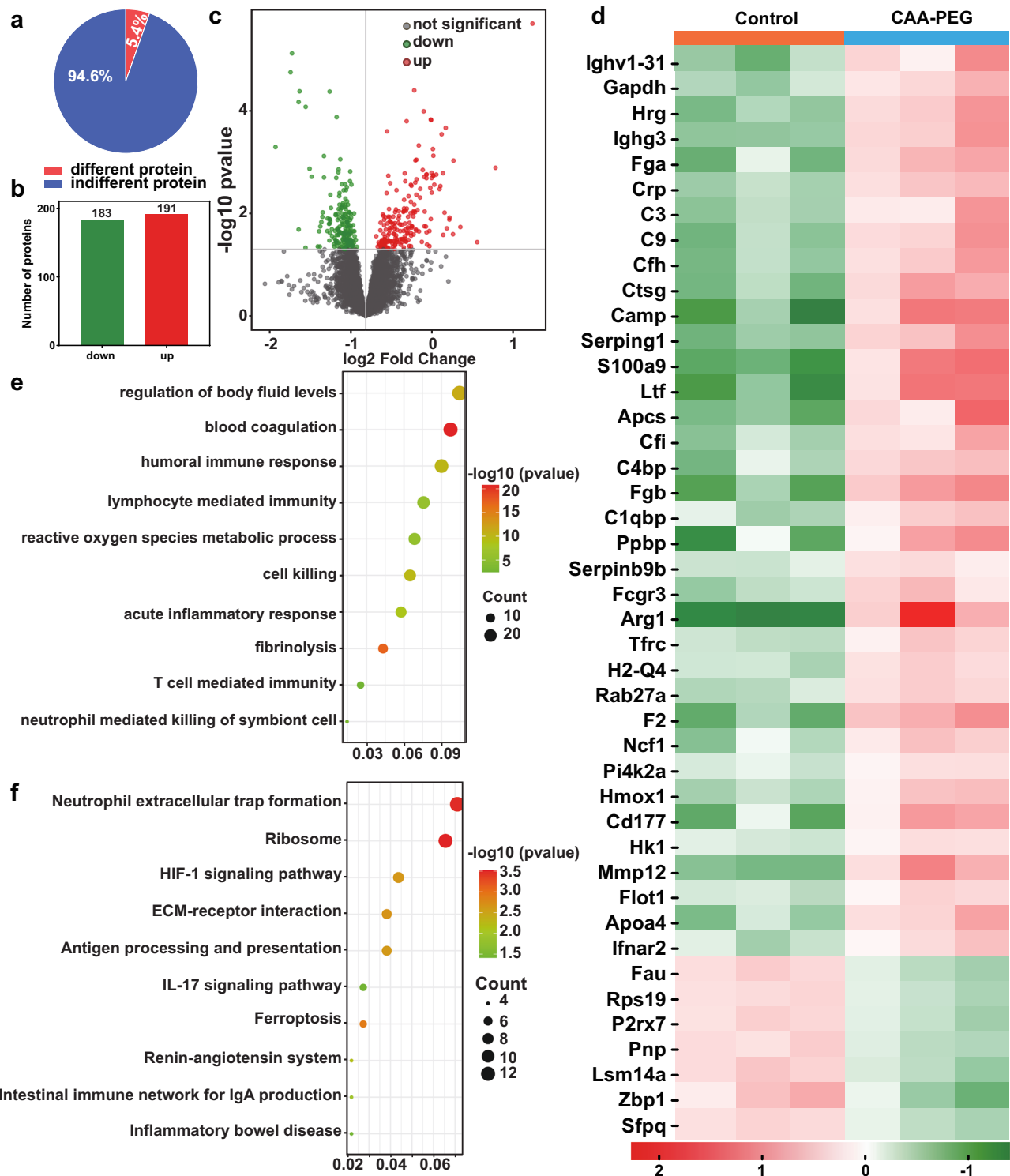
Fig. 7 | The mechanisms of CAA-PEG NSs-mediated H₂S depletion in inducing anti-tumor immunotherapy. a Proportion of differential protein and non-differential protein. Column (**b**) and volcano maps (**c**) of upregulated and downregulated proteins in differential proteins. **d** The heat map of differential immune-related proteins. The GO enrichment analysis (**e**) and the KEGG pathway enrichment analysis (**f**) of differential proteins related to immune processes. No multiple comparisons were made. The data are presented as mean values +/− SD, $n = 3$ mice.

demonstrating specific immune effects related to anti-tumor response were triggered after CAA-PEG NSs treatment. Subsequently, the Kyoto Encyclopedia of Genes and Genomes (KEGG) pathway analysis revealed that the most significant pathways included Hypoxia Inducible Factor-1 (HIF-1) signaling pathway[39], antigen processing and presentation, renin-angiotensin system[40], and interleukin 17 (IL-17) signaling pathway[41] (Fig. 7f), which are an essential role to activate the

immune function. In addition, we found significant enrichment of the ferroptosis signaling pathway and reactive oxygen species metabolic process (GO process). Moreover, the nuclear factor IFN homologous proteins (IFNar2), critical in promoting M1 TAMs polarization, was remarkably upregulated in response to CAA-PEG NSs treatment[42]. Based on the above results, reactive oxygen species (ROS) may lead M2 macrophages to M1 macrophages transformation. High expression of

antigen presentation and effector T cell-related proteins H2-Q4[43], lgmn[44], Arg1[45] in CAA-PEG NSs-treated tumors. These results indicated that CAA-PEG NSs could induce DC maturation, T cell activation and infiltration after Inhibition of endogenous H_2S production in the CRC microenvironment.

Discussion

The tumor microenvironment harbors many cell types, including fibroblasts, immune cells, and other components contributing to malignant behavior and progression[46]. Conventional therapies such as chemotherapy, radiation, and surgery always fail for the microenvironment-mediated drug resistance, metastasis, or relapse in the clinic[47,48]. Multi-modal therapeutic strategies not only kill malignant tumor cells via conventional treatments, but also remodel the tumor microenvironment and eradicate the potential unfavorable factors, including drug resistance and immunosuppression[49]. In the tumor microenvironment of colon cancer, high level of endogenous H_2S is a key feature and a major cause of "cold tumors"[20,50]. In this study, we have exploited the strategy of reduced H_2S-mediated arsenic valence transition to develop arsenic-based nanosheets.

Under the H_2S-abundant CRC microenvironment, the PEGylated arsenic nanosheets rapidly dissociated, and released As^V, AOAA, and Cu^{2+}, thereby triggering a cascade of synergistic effects:

1. Low systemic toxicity As^V is reduced to the therapeutic state As^{III} to exert its chemotherapy. Through this mechanism, we are able to significantly broaden the therapeutic window of arsenic compounds, rendering them promising chemotherapeutic agents for solid tumors;

2. Simultaneously, the H_2S depletion during the conversion of As^V to As^{III} and the AOAA-mediated inhibition and/or downregulation of H_2S-producing enzymes completely remodel the immunosuppressive microenvironments by inducing maturation and differentiation of immune cells to generate more tumor-killing T-cells, as well as repolarization of M2 into M1 tumor-associated macrophages;

3. As a by-product of nanosheet decomposition, the generation of ultrasmall CuS NPs guided by photoacoustic imaging has a strong NIR-II absorption capacity, which is a powerful complement to CRC chemotherapy. Consequently, the synergistic effect of chemotherapy with photothermal therapy was maximized in our study.

Although arsenic-based 2D nanomaterials, such as arsenic-phosphorus nanosheets[51] and arsenene nanosheets[52,53], show promise in cancer treatment, they face challenges including potential toxicity to normal tissues, complex and costly synthesis, and stability issues during storage and transport. Our development of in situ valence-transited arsenic nanosheets offers a highly efficient multi-modal therapeutic platform specifically designed for colorectal cancer. This approach integrates chemotherapy, photothermal therapy, and immune microenvironment remodeling, effectively addressing the multifaceted challenges of CRC treatment. Our method demonstrates comprehensive suppression of CRC progression and prevention of recurrence. While our study is currently limited to a single murine CRC cell line, the successful development of CAA-PEG NSs underscores the potential of valence-transited arsenic-based therapeutic strategies for CRC treatment.

Methods

Ethics statement

Female BALB/c mice (3–5 weeks, 18 ± 2 g) were purchased from SLAC Laboratory Animal Co. Ltd. (Shanghai, China). All experiments were performed under experimental protocols approved by the Animal Care and Use Committee of Zhejiang Chinese Medical University (No. 201909-0415). Animal ethics states that the weight of tumors in mice should not exceed 10% of the mouse's body weight, and the size of tumors should not exceed 15 mm in any dimension. It was confirmed that all the maximal tumor size/burden was not exceeded. The environmental conditions in the mouse facility were: 12 h light/dark cycle (light on from 8:00 a.m. to 8:00 p.m.), temperature range of $22 \pm 2 \, ^\circ C$, relative humidity range of $50\% \pm 10\%$, and free access to food and water.

Materials

Sodium arsenate dibasic heptahydrate ($Na_2HAsO_4 \cdot 7H_2O$), Copper chloride dihydrate ($CuCl_2 \cdot 2H_2O$, 99%) was purchased from Sigma-Aldrich (USA). Aminooxyacetic acid (AOAA, 95%) was purchased from Beijing Qisong Biotechnology Co., Ltd (Beijing, China). NH_2-PEG-COOH (MW: 3400 Da) and nitric acid (65–68%) were purchased from Aladdin (Shanghai, China). Sodium hydrosulfide (NaHS, 68–72%) was purchased from Ourchem (Shanghai, China). 3,3',5,5'-Tetramethylbenzidine (TMB) was purchased from Solarbio Science & Technology Co., Ltd (Beijing, China). 4',6-diamidino-2-phenylindole (DAPI), cell counting kit (CCK-8) and BCA protein kit was bought from Beyotime (Shanghai, China).7-Azido-4-methylcoumarin (AzMC) was bought from Dehang Wuzhou Technology Co., Ltd (Beijing, China). RIPA buffer and Protein Free Rapid blocking buffer (5×) was bought from Yamei Biopharmaceutical Technology Co., Ltd (Shanghai, China). TNF-α, IFN-γ, IL-6, IL-10, IL-1β, VEGF, and bFGF ELISA kits was bought from Fiya Biotechnology Co., Ltd (Jiangsu, China). Mouse colon cancer cells (CT-26, ATCC® number: CRL-2638™, Lot number: 70016788) was purchased from American Type Culture Collection (ATCC). Cells have been genotyped for STR and routinely tested for mycoplasma. Relevant supporting documentation can be viewed in the Supplementary Materials.

Preparation of CAA-PEG NSs

Arsenic nanosheets (CAA NSs) were prepared using a one-pot self-assembly method. Briefly, 312 mg $Na_2HAsO_4 \cdot 7H_2O$, 170 mg $CuCl_2 \cdot H_2O$ and 18 mg AOAA were each dissolved in 25 mL of ultrapure water, respectively. The three solutions were then stirred violently at 4 °C for 30 min, followed by transfer to hydrothermal autoclave for 30 min at 180 °C. CAA NSs was collected by washing by centrifugation ($8000 \times g$, 10 min) for three times. 20 mL of NH_2-PEG-COOH (8.33 mg/mL) was added to the previously prepared CAA NSs solution and the mixture was stirred overnight to obtain CAA-PEG NSs.

Characterization of CAA-PEG NSs

The morphology and elemental mapping spectra of CAA-PEG NSs were observed with transmission electron microscopy (JEM 2100F, JEOL, Japan). Atomic force microscope (Bruker Dimension Icon, DEU) was used to observe CAA-PEG NSs thickness. The zeta potentials of CAA NSs and CAA-PEG NSs were measured by Malvern laser particle size analyzer (Nano-ZS90, UK). AOAA content was determined with ninhydrin colorimetric method. As and Cu contents were determined by inductive coupled plasma emission spectroscopy (ICP, 6300, Thermo Electron Corporation, USA).

Structural preparation

Construct the three-dimensional structures of AOAA and arsenate molecules, and perform structural optimization using the MMFF94 force field[54]. Then, further refine the structure using ORCA, calculating the force field parameters[55]. During optimization, the B97-3c functional is used[56]. After optimization, the atomic charges are fitted using the RESP method, and the GAFF force field parameters are generated using Multiwfn and Sobtop[57–60].

Molecular dynamics simulation

The system was constructed using Packmol[61] and Gromacs 2021.7[62,63], with the Amber99sb and GAFF force fields. The water model used was

SPC[64]. The simulation was carried out at a temperature of 453.15 K and a pressure of 2 MPa using Gromacs 2021.7[65–68]. The simulation box size was set to $10 \times 10 \times 10$ nm³. Packmol was used to randomly place 60 Na_2HAsO_4 molecules, 60 $CuCl_2$ molecules, and 12 AOAA molecules into the box, which was then filled with water (a total of 32,156 water molecules). The molecular quantities were calculated based on the molar ratios used in the actual experiments, and specific comparisons can be found in the Table S1 (Supplementary Info). Before the production run, energy minimization, 100 ps NVT pre-equilibration, and 100 ps NPT pre-equilibration were performed sequentially. After the system relaxed, a 100 ns production simulation was executed. The production simulation used the leapfrog algorithm to integrate Newton's equations of motion with a time step of 2 fs. The V-rescale method was used for temperature coupling, and the Parrinello-Rahman method was used for pressure coupling[69]. The Verlet method[70] was employed for neighbor searching, with a cutoff radius of 1.4 nm for Coulomb and van der Waals interactions. The Particle Mesh Ewald (PME) method was used for long-range electrostatics[71,72], and long-range dispersion corrections were applied to the energy and pressure. The entire molecular dynamics process was conducted independently three times, with no data carried over from any specific NVT or NPT equilibration. Each process and its corresponding results were entirely independent of the others. We performed data extraction and analysis, including hydrogen bonds, interaction forces, and RMSD values, using standard procedures from the Gromacs toolkit. All system setups and subsequent analysis methods can be found in the official Gromacs documentation: https://manual.gromacs.org/.

The RMSD analysis command: gmx rms -s md.tpr -f md.xtc -o rmsd.xvg.

The H-bond analysis command: gmx hbond -f md.xtc -s md.tpr -n index.ndx -num.

Dissociation of CAA-PEG NSs under sodium hydrosulfide
NaHS was used to simulate endogenous H_2S[73]. Follow the product instructions, the NaHS solid was dissolved in ddH_2O and filtered to obtain a fresh 3 mM solution of NaHS. CAA-PEG NSs (Cu: 80 µg/mL) were added to NaHS solution for a certain time and then centrifuged to collect at different time points (15, 60, and 120 min). Nanoparticles were characterized by Electronic Differential System (EDS) and TEM.

Vis-NIR absorption, photothermal effect and photoacoustic performance of CAA-PEG NSs in the existence of NaHS
After the reaction of CAA-PEG NSs (Cu: 80 µg/mL) with different concentrations of NaHS (0, 0.5, 1, 2, and 3 mM) for 2 h, the Vis-NIR absorption was measured by an ultraviolet/visible/near infrared spectrophotometer (Shimadzu, UV-3600, Japan), and the photoacoustic image signal was detected with photoacoustic imaging system (InVision256-TF). Infrared (IR) thermal camera (ICI 7320, Infrared Camera Inc., Beaumont, TX, USA) was used to record the temperature change of CAA-PEG NSs reaction with different concentrations of NaHS under the irradiation of 1064 nm laser to study the photothermal effect. Certain concentrations of CAA-PEG NSs (Cu: 80 µg/mL) and NaHS were subjected to multiple rounds of illumination (1064 nm, 5 min on/off) to record the temperature changes.

H_2S-triggered release and valence transit of arsenic from CAA-PEG NSs
CAA-PEG NSs (Cu: 80 µg/mL) solution was loaded into a dialysis bag (MW: 3500 Da) with release medium containing NaHS and was oscillated in an air bath at 37 °C. ICP was used to determine the arsenic released from CAA-PEG NSs within a specified time interval. The transit of arsenic valence in solution was detected by X-ray photoelectron spectroscopy (XPS, Thermo Scientific K-Alpha, USA) after CAA-PEG NSs were mixed with different concentrations (0, 1, 2 mM) of NaHS for 2 h.

Cellular uptake and intracellular degradation of CAA-PEG NSs
For cellular uptake study, CT-26 cells were cultured in laser confocal dishes and incubated with free ICG or ICG-labelled CAA-PEG NSs for 4 h. Cells were washed with PBS, fixed with 4% paraformaldehyde, stained with DAPI, and observed by confocal laser scanning microscope (CLSM) (LSM880, Carl Zeiss, GER).

Intracellular degradation of CAA-PEG NSs was observed by bio-TEM. First, CT-26 cells (5×10^5 cells/well) were cultured in 6-well plate at 37 °C. Subsequently, the medium was replaced with fresh culture medium containing CAA-PEG NSs. Then, bio-TEM images of cells were obtained after frozen section at 1, 3, and 6 h.

CLSM and Flow cytometer (FCM, BD LSRFortessa, USA) were used to observe the changes of H_2S in CT-26 cells. CT-26 cells were cultured in laser confocal dishes and incubated with CAA-PEG NSs for 4, 12, and 24 h (without CAA-PEG NSs in the control group). Cells were washed with PBS, and stained with AzMC for 30 min[18,31]. CLSM and flow cytometry (FCM) were used to observe fluorescence intensity.

In vitro cytotoxicity and cell apoptosis assay
CCK-8 was used to evaluate the in vitro cytotoxicity of CAA-PEG NSs. Briefly, CT-26 cells (1×10^4 cells/well) were cultured in 96-well plates overnight and replaced with fresh culture medium containing CAA-PEG NSs with different concentrations for 24 h. The 1064 nm laser (1.0 W/cm², 5 min) was used to treat irradiated groups.

For live/dead cell staining, CT-26 cells (5×10^5 cells/well) were cultured in laser confocal dishes and incubated with culture medium or CAA-PEG NSs (As: 15 µg/mL) for 6 h, the 1064 nm laser (1.0 W/cm², 5 min) was used to treat with irradiated groups. CLSM was used to observe the Calcein-AM and PI co-staining.

For cell apoptosis assay, CT-26 cells (5×10^5 cells/well) were cultured in 6-well plates and incubated with culture medium or CAA-PEG NSs (As: 15 µg/mL) for 6 h, the 1064 nm laser (1 W/cm², 5 min) was used to treat with irradiated groups. FCM was used to observe the result of Annexin-FITC and PI co-staining.

Intracellular transit of arsenic valence
CT-26 cells (5×10^5 cells/well) were cultured in 6-well plates and incubated with culture medium containing CAA-PEG NSs (As: 15 µg/mL) for 12 h. Afterwards, the CT-26 cells were washed 3 times with PBS, freeze-thawed 3 times at −20/37 °C, sonicated for 5 min in 5% HNO_3 solution and centrifuged to collect the arsenic-containing solution. Finally, the arsenic valence was evaluated by atomic fluorescence spectroscopy (AFS).

Western blot analysis
RIPA buffer was used to lyse CT-26 cells. BCA protein kit was used to normalize the protein concentrations. The proteins were isolated applying wet electroblotting systems (Bio-Rad) by SDS-PAGE and transferred to PVDF membranes (Beyotime). The PVDF membranes were blocked in protein free rapid blocking buffer for 30 min and incubated with primary antibodies overnight at 4 °C. Antibodies against the following proteins were used for the western blot assay: β-actin (Proteintech, Cat 66009), P53 (Proteintech, Cat 60283-2-lg), P21 (Abcam, ab109199), CSE (Proteintech, Cat 60234-1-Ig), CBS (Proteintech, Cat 67861-1-Ig), 3-MST (Abcam, ab317833) and CAT (Abcam, ab189863). ECL Substrate was used to perform signal detection. QuickChemi 5200 system (Monad) was used to collect and analyze the signals.

In vivo imaging and biodistribution study
Female BALB/c mice (3–5 weeks, 18 ± 2 g) were purchased from SLAC Laboratory Animal Co. Ltd. (Shanghai, China). When the tumor volumes reached 100 mm³, ICG and CAA-PEG-ICG were injected into mice intravenously. The ICG fluorescence was observed by in vivo imaging system (excitation: 710 nm, filter: 745 nm; IVIS, PerkinElmer, Waltham, MA, USA) at specific time points (1, 2, 4, 8, 12, and 24 h). After

24 h injection, mice were sacrificed, and the biodistribution imaging was used to observe the fluorescence intensity in tumors and major organs.

To establish the in-situ murine model of colon cancer, the mice were prepared as previously described and intracecum injections (5×10^5 CT-26 cells suspended in 25 µL of PBS) were performed using an insulin-gauge syringe. Then, the mice were injected with 100 µL of saline, free As (V), free As (III), CA-PEG NSs and CAA-PEG NSs (As: 1 mg/kg) ($n = 4$) through a tail vein. All mice were injected intravenously with the above formulations through the tail vein once a day for 10 days. During the treatment period, the body weight, tumor weight and tumor diameter of mice in each group were recorded every week. After 24 days of treatment, the mice in each group were euthanized for the collection of tumors.

In vivo transit of arsenic valence
CT-26 tumor-bearing mice were injected with CAA-PEG NSs (As: 1 mg/kg) ($n = 3$). The mice were sacrificed after 24 h, and the major organs were collected. The organs were kept in nitric acid overnight and centrifuged at $8000 \times g$ for 15 min. The supernatant was mixed with equal n-hexane, shaken for 1 min, and centrifuged for 15 min. The n-hexane was removed, and the obtained liquid was filtered through 0.45 µm organic membrane. Finally, AFS and ICP were used to evaluate the arsenic valence in the extracted solution.

In vivo photoacoustic imaging and photothermal effect
CT-26 tumor-bearing mice were injected with 100 µL CAA-PEG NSs (As: 1 mg/kg) through a tail vein for in vivo PA imaging. All of the PA imaging was obtained using the photoacoustic imaging system. The photoacoustic signal of the control group was replaced by the pre-injection.

CT-26 tumor-bearing mice were injected with 100 µL saline, CA-PEG NSs and CAA-PEG NSs (As: 1 mg/kg). After 8 h, mice were anesthetized by intraperitoneal injection of 0.3% pentobarbital sodium (0.25 mL/10 g). The tumor site was irradiated with 1064 nm near-infrared laser at 1 W/cm^2 for 10 min. The temperature changes in the tumor site were recorded by IR thermal camera.

In vivo anti-tumor efficacy and biosafety studies
CT-26 tumor-bearing mice were injected with saline, free As (V), free As (III), CA-PEG NSs, CAA-PEG NSs, CA-PEG NSs+Laser, CAA-PEG NSs +Laser (As: 1 mg/kg) ($n = 6$) through a tail vein. The 1064 nm laser (1.0 W/cm^2, 10 min) was used to treat with irradiated groups after 8 h. The treatment process was repeated every other day for 3 cycles. Tumor size and the survival of mice were recorded every other day.

CT-26 tumor-bearing mice were injected with 100 µL saline, free As (V), free As (III), CA-PEG NSs and CAA-PEG NSs (As: 1 mg/kg), and the mice were sacrificed following three doses. Tumor samples were collected and fixed. Tissue blocks were processed for immuno-fluorescence (IF) analysis. The tumors were stained with primary antibodies against the following proteins: CBS (Proteintech, Cat 67861-1-Ig), P53 (Proteintech, Cat 60283-2-lg), PE-CD86 (Proteintech, Cat PE-65068), PE-CD8 (Proteintech, Cat PE-65069), Dylight 594-Goat Anti Mouse IgG (Immunoway, RS23410). These pathological sections were observed by VS120-S6-W system (OLYMPUS, JPN).

For DC maturation, T cell activation, and macrophage polarization analysis, tumors were collected, homogenized, and filtered to obtain a single cell suspension in PBS after the above treatment. The tumor cell suspension was then stained with APC-F4/80 (Biolegend, Cat 123116), PE-CD86, FITC-CD206 (Biolegend, Cat 141703), APC-CD11 (Proteintech, Cat APC-65130), FITC-CD80 (Proteintech, Cat FITC-65076), FITC-CD3 (Proteintech, Cat FITC-65077), PE-CD8 (Proteintech, Cat PE-65068), and APC-CD4 (Proteintech, Cat APC-65141) antibodies for cell phenotype analysis by FCM. The gating strategy has been provided in Supplementary Fig. 26. Spleens were collected for T cell activation analysis. The staining method was the same as above. Similarly, mouse serum was obtained, and the content of cytokines (TNF-α, IFN-γ, IL-6, IL-10, IL-1β, VEGF, and bFGF) in serum was measured using ELISA kits.

The biosafety study was implemented by injecting saline, free As (V), free As (III), CA-PEG NSs, CAA-PEG NSs, CA-PEG NSs+Laser, CAA-PEG NSs+Laser (100 µL, 1 mg/kg) into the BALB/c mice ($n = 3$) intravenously. After three doses, blood from these mice was obtained for routine blood test and biochemical analysis.

Proteomics analysis
For TMT-based proteomics analysis, tumor tissues were collected from each treatment group. Protein extraction and quantization were performed with BCA kit. The protein samples were subjected to SDS-PAGE electrophoresis to examine the consistency of each group. Next, 120 µg of protein sample from each group was reduced, alkylated, digested with trypsin (1 µg/µL) at 37 °C overnight. Then, the tryptic peptide solution of each sample was labeled according to the TMT labeling reagent instructions. The dry samples were re-suspended with 100 µL of buffer A (2% acetonitrile, 98% water, ammonia water adjusted to pH = 10), and the reverse phase liquid chromatography (RPLC) was conducted on the L-3000 HPLC (RIGOL, China). The parameters used were a Waters BEH C18 (4.6 × 250 mm, 5 µm) column. Separation was performed at 1 mL/min using a nonlinear binary gradient starting with buffer A and transitioning to buffer B (98% acetonitrile, 2% water, ammonia water adjusted to pH = 10). Samples were collected at minute intervals starting from 1 min, 10 samples were pooled and collected. Each sample was dried in a vacuum freeze dryer for RPLC-MS/MS analysis of the TMT-labeled samples. The Easy-nLC™ 1200 System (Thermo Scientific, USA) was used for the online RPLC detection. The Q Exactive™ System (Thermo Scientific, USA) was used for mass spectrometry. Peptides were quantitatively identified according to the peak signal intensity and the secondary mass spectrometry information of different reporter ions of the TMT tag reagents. Groups were analyzed in triplicate to minimize the effect of individual differences.

Statistics & reproducibility
Number of experimental replicates (n) is indicated in figure legend and refers to the number of experimental subjects independently treated in each experimental condition. No statistical methods were used to pre-determine sample size, or to randomize. One-way or Two-way ANOVA tests were used when comparing two or more than two normally distributed data sets. Statistical analyses were carried out using GraphPad Prism (version 10.4.0). A statistical significance threshold was set at 0.05, and significance levels are presented as *$P < 0.05$, **$P < 0.01$, P values less than 0.001 were presented in absolute values in the figures.

Reporting summary
Further information on research design is available in the Nature Portfolio Reporting Summary linked to this article.

Data availability
The mass spectrometry proteomics data have been deposited to the ProteomeXchange Consortium via the PRIDE[74] partner repository with the dataset identifier PXD059728. Reviewers can log in to the PRIDE website (http://www.ebi.ac.uk/pride) using the following details: Project accession: PXD059728; Token: n6pFdYeYrozW to review the data. All other data supporting this work is available from the Article, Supplementary Information or source data file. Source data file is provided with this paper. Source data are provided with this paper.

References

1. Schmitt, M. & Greten, F. R. The inflammatory pathogenesis of colorectal cancer. *Nat. Rev. Immunol.* **21**, 653 (2021).
2. Schonkeren, S. L., Thijssen, M. S., Vaes, N., Boesmans, W. & Melotte, V. The emerging role of nerves and glia in colorectal cancer. *Cancers (Basel).* **13**, 152 (2021).
3. Miller, K. D. et al. Cancer treatment and survivorship statistics, 2022. *CA Cancer J. Clin.* **72**, 409 (2022).
4. Emadi, A. & Gore, S. D. Arsenic trioxide - An old drug rediscovered. *Blood Rev.* **24**, 191 (2010).
5. Cui, Z. et al. Nanodiamond autophagy inhibitor allosterically improves the arsenical-based therapy of solid tumors. *Nat. Commun.* **9**, 4347 (2018).
6. Sonksen, M., Kerl, K. & Bunzen, H. Current status and future prospects of nanomedicine for arsenic trioxide delivery to solid tumors. *Med. Res. Rev.* **42**, 374 (2022).
7. Garbinski, L. D., Rosen, B. P. & Chen, J. Pathways of arsenic uptake and efflux. *Environ. Int.* **126**, 585 (2019).
8. Li, C. et al. MMP2-responsive dual-targeting drug delivery system for valence-controlled arsenic trioxide prodrug delivery against hepatic carcinoma. *Int. J. Pharm.* **609**, 121209 (2021).
9. Vega, L. et al. Differential effects of trivalent and pentavalent arsenicals on cell proliferation and cytokine secretion in normal human epidermal keratinocytes. *Toxicol. Appl. Pharmacol.* **172**, 225 (2001).
10. Cao, X. et al. A review of hydrogen sulfide synthesis, metabolism, and measurement: is modulation of hydrogen sulfide a novel therapeutic for cancer? *Antioxid. Redox. Signal.* **31**, 1 (2019).
11. Szabo, C. et al. Tumor-derived hydrogen sulfide, produced by cystathionine-beta-synthase, stimulates bioenergetics, cell proliferation, and angiogenesis in colon cancer. *Proc. Natl. Acad. Sci. USA* **110**, 12474 (2013).
12. Ascenção, K., Lheimeur, B. & Szabo, C. Regulation of CyR61 expression and release by 3-mercaptopyruvate sulfurtransferase in colon cancer cells. *Redox Biol.* **56**, 102466 (2022).
13. Li, Y. et al. H_2S-scavenged and activated iron oxide-hydroxide nanospindles for MRI-guided photothermal therapy and ferroptosis in colon cancer. *Small.* **16**, e2001356 (2020).
14. Chen, J. et al. An endogenous H_2S-activated nanoplatform for triple synergistic therapy of colorectal cancer. *Nano Lett.* **22**, 6156 (2022).
15. Chen, H. J. et al. Recent advances in the role of endogenous hydrogen sulphide in cancer cells. *Cell Prolif.* **56**, e13449 (2023).
16. Chen, S. et al. Inhibition of hydrogen sulfide synthesis reverses acquired resistance to 5-FU through miR-215-5p-EREG/TYMS axis in colon cancer cells. *Cancer Lett.* **466**, 49 (2019).
17. Rahman, M. A. et al. Hydrogen sulfide dysregulates the immune response by suppressing central carbon metabolism to promote tuberculosis. *Proc. Natl. Acad. Sci. USA* **117**, 6663 (2020).
18. Dong, X. et al. Depletion and downregulation of hydrogen sulfide using an activatable probe for promoting photothermal therapy toward colorectal cancers. *J. Med. Chem.* **67**, 7431 (2024).
19. Asimakopoulou, A. et al. Selectivity of commonly used pharmacological inhibitors for cystathionine β synthase (CBS) and cystathionine γ lyase (CSE),. *Br. J. Pharmacol.* **169**, 922 (2013).
20. Lin, H. et al. Implications of hydrogen sulfide in colorectal cancer: mechanistic insights and diagnostic and therapeutic strategies. *Redox Biol.* **59**, 102601 (2023).
21. Chen, H. et al. Lipid encapsulation of arsenic trioxide attenuates cytotoxicity and allows for controlled anticancer drug release. *J. Am. Chem. Soc.* **128**, 13348 (2006).
22. Liu, C. et al. The osteogenic niche-targeted arsenic nanoparticles prevent colonization of disseminated breast tumor cells in the bone. *Acta Pharm. Sin. B.* **12**, 364 (2022).
23. Ahn, R. W. et al. A novel nanoparticulate formulation of arsenic trioxide with enhanced therapeutic efficacy in a murine model of breast cancer. *Clin. Cancer Res.* **16**, 3607 (2010).
24. Lee, S. M., Lee, O. S., O'Halloran, T. V., Schatz, G. C. & Nguyen, S. T. Triggered release of pharmacophores from [Ni(HAsO$_3$)]-loaded polymer-caged nanobin enhances pro-apoptotic activity: a combined experimental and theoretical study. *ACS Nano.* **5**, 3961 (2011).
25. Fan, L. et al. Dual oligopeptides modification mediates arsenic trioxide containing nanoparticles to eliminate primitive chronic myeloid leukemia cells inside bone marrow niches. *Int. J. Pharm.* **579**, 119179 (2020).
26. Kallinteri, P., Fatouros, D., Klepetsanis, P. & Antimisiaris, S. G. Arsenic trioxide liposomes: encapsulation efficiency and in vitro stability. *J. Liposome Res.* **14**, 27 (2004).
27. Barua, S. & Mitragotri, S. Challenges associated with penetration of nanoparticles across cell and tissue barriers: a review of current status and future prospects. *Nano Today.* **9**, 223 (2014).
28. Chhowalla, M., Liu, Z. & Zhang, H. Two-dimensional transition metal dichalcogenide (TMD) nanosheets. *Chem. Soc. Rev.* **44**, 2584 (2015).
29. Rodenas, T. et al. Metal-organic framework nanosheets in polymer composite materials for gas separation. *Nat. Mater.* **14**, 48 (2015).
30. Augsburger, F. et al. Role of 3-mercaptopyruvate sulfurtransferase in the regulation of proliferation, migration, and bioenergetics in murine colon cancer cells. *Biomolecules.* **10**, 447 (2020).
31. Dong, X. et al. An injectable and adaptable hydrogen sulfide delivery system for modulating neuroregenerative microenvironment. *Sci. Adv.* **9**, eadi1078 (2023).
32. Ascenção, K. et al. Pharmacological induction of mesenchymal-epithelial transition via inhibition of H_2S biosynthesis and consequent suppression of ACLY activity in colon cancer cells. *Pharmacol. Res.* **165**, 105393 (2021).
33. Bantzi, M. et al. Novel aryl-substituted pyrimidones as inhibitors of 3-mercaptopyruvate sulfurtransferase with antiproliferative efficacy in colon cancer. *J. Med. Chem.* **64**, 6221–6240 (2021).
34. Szabo, C. & Papapetropoulos, A. International union of basic and clinical pharmacology. CII: pharmacological modulation of H2S levels: H2S donors and H2S biosynthesis inhibitors. *Pharmacol. Rev.* **69**, 497–564 (2017).
35. Chang, M. et al. Colorectal tumor microenvironment-activated bio-decomposable and metabolizable Cu(2)O@CaCO(3) nanocomposites for synergistic oncotherapy. *Adv. Mater.* **32**, e2004647 (2020).
36. Liu, Y., Bhattarai, P., Dai, Z. & Chen, X. Photothermal therapy and photoacoustic imaging via nanotheranostics in fighting cancer. *Chem. Soc. Rev.* **48**, 2053 (2019).
37. Thanki, K. K. et al. Deletion of cystathionine-γ-lyase in bone marrow-derived cells promotes colitis-associated carcinogenesis. *Redox Biol.* **55**, 102417 (2022).
38. Youness, R. A. et al. Targeting hydrogen sulphide signaling in breast cancer. *J. Adv. Res.* **27**, 177 (2021).
39. Jing, X. et al. Role of hypoxia in cancer therapy by regulating the tumor microenvironment. *Mol. Cancer.* **18**, 157 (2019).
40. Nataraj, C. et al. Angiotensin II regulates cellular immune responses through a calcineurin-dependent pathway. *J. Clin. Invest.* **104**, 1693 (1999).
41. Deng, R. H. et al. Nanoparticles from cuttlefish ink inhibit tumor growth by synergizing immunotherapy and photothermal therapy. *ACS Nano.* **13**, 8618 (2019).
42. He, L. et al. Global characterization of macrophage polarization mechanisms and identification of M2-type polarization inhibitors. *Cell Rep.* **37**, 109955 (2021).
43. Li, H. et al. Comprehensive exome analysis of immunocompetent metastatic head and neck cancer models reveals patient relevant landscapes. *Cancers (Basel).* **12**, 2935 (2020).

44. Shen, L. et al. Legumain-deficient macrophages promote senescence of tumor cells by sustaining JAK1/STAT1 activation. *Cancer Lett.* **472**, 40 (2020).

45. Aaboe Jorgensen, M. et al. Arginase 1-based immune modulatory vaccines induce anticancer immunity and synergize with anti-PD-1 checkpoint blockade. *Cancer Immunol. Res.* **9**, 1316 (2021).

46. Lei, X. et al. Immune cells within the tumor microenvironment: biological functions and roles in cancer immunotherapy. *Cancer Lett.* **470**, 126 (2020).

47. Fares, J., Fares, M. Y., Khachfe, H. H., Salhab, H. A. & Fares, Y. Molecular principles of metastasis: a hallmark of cancer revisited. *Signal Transduct. Target. Ther.* **5**, 28 (2020).

48. Vasan, N., Baselga, J. & Hyman, D. M. A view on drug resistance in cancer. *Nature.* **575**, 299 (2019).

49. Aldea, M. et al. Overcoming resistance to tumor-targeted and immune-targeted therapies. *Cancer Discov.* **11**, 874 (2021).

50. Yue, T. et al. Hydrogen sulfide creates a favorable immune microenvironment for colon cancer. *Cancer Res.* **83**, 595 (2023).

51. Hu, R. et al. Engineering 2D arsenic-phosphorus theranostic nanosheets. *Adv. Funct. Mater.* **31**, 2101660 (2021).

52. Wang, X. et al. Multi-omics analysis reveals the unexpected immune regulatory effects of arsenene nanosheets in tumor microenvironment. *ACS Appl. Mater. Interfaces.* **14**, 45137–45148 (2022).

53. He, P. et al. Anti-Her2 affibody-decorated arsenene nanosheets induce ferroptosis through depleting intracellular GSH to overcome cisplatin resistance. *J. Nanobiotechnology.* **21**, 203 (2023).

54. Tosco, P., Stiefl, N. & Landrum, G. Bringing the MMFF force field to the RDKit: implementation and validation. *J. Chem. Inform.* **6**, 37 (2014).

55. Neese, F. The ORCA program system. *Wiley Interdiscip Rev. Comput. Mol. Sci.* **2**, 73–78 (2012).

56. Brandenburg, J. G., Bannwarth, C., Hansen, A. & Grimme, S. B97-3c: a revised low-cost variant of the B97-D density functional method. *J. Chem. Phys.* **148**, 064104 (2018).

57. Lu, T. Sobtop Version [1.0(dev3)]. http://sobereva.com/soft/Sobtop (2023).

58. Schauperl, M. et al. Non-bonded force field model with advanced restrained electrostatic potential charges (RESP2). *Commun. Chem.* **3**, 44 (2020).

59. Lu, T. & Chen, F. Multiwfn: a multifunctional wavefunction analyzer. *J. Comput. Chem.* **33**, 580 (2012).

60. Wang, J., Wolf, R. M., Caldwell, J. W., Kollman, P. A. & Case, D. A. Development and testing of a general amber force field. *J. Comput. Chem.* **25**, 1157 (2004).

61. Martínez, L., Andrade, R., Birgin, E. G. & Martínez, J. M. PACKMOL: a package for building initial configurations for molecular dynamics simulations. *J. Comput. Chem.* **30**, 2157–2164 (2009).

62. Pronk, S. et al. GROMACS 4.5: a high-throughput and highly parallel open source molecular simulation toolkit. *Bioinformatics.* **29**, 845 (2013).

63. Abraham, M. J. et al. GROMACS: high performance molecular simulations through multi-level parallelism from laptops to supercomputers. *SoftwareX.* **1**, 19 (2015).

64. Mark, P. & Nilsson, L. Structure and dynamics of the TIP3P, SPC, and SPC/E water models at 298 K. *J. Phys. Chem. A.* **105**, 9954 (2001).

65. Akbayrak, I. Y. et al. Structures of MERS-CoV macro domain in aqueous solution with dynamics: Impacts of parallel tempering simulation techniques and CHARMM36m and AMBER99SB force field parameters. *Proteins.* **89**, 1289–1299 (2021).

66. Yutani, K., Matsuura, Y. & Joti, Y. Confirmation of the formation of salt bridges in the denatured state of CutA1 protein using molecular dynamics simulations. *Biophys. Physicobiol.* **16**, 176–184 (2019).

67. Papavasileiou, K. D., Moultos, O. A. & Economou, I. G. Predictions of water/oil interfacial tension at elevated temperatures and pressures: A molecular dynamics simulation study with biomolecular force fields. *Fluid Phase Equilibr.* **476**, 30–38 (2018).

68. Sharifipour, M. & Nakhaee, A. Molecular dynamics simulation of methane hydrates: Prediction of the phase equilibria using extracted microscopic parameters from SAFT-VR Mie EOS. *Fluid Phase Equilibr.* **582**, 114100 (2024).

69. Samantray, S., Yin, F., Kav, B. & Strodel, B. Different force fields give rise to different amyloid aggregation pathways in molecular dynamics simulations. *J. Chem. Inf. Model.* **60**, 6462 (2020).

70. Chialvo, A. A. & Debenedetti, P. G. On the use of the Verlet neighbor list in molecular dynamics. *Comput. Phys. Commun.* **60**, 215 (1990).

71. Kabedev, A., Bergström, C. A. S. & Larsson, P. Molecular dynamics study on micelle-small molecule interactions: developing a strategy for an extensive comparison. *J. Comput. Aided. Mol. Des.* **38**, 5 (2023).

72. Darden, T., York, D. M. & Pedersen, L. G. Particle mesh Ewald: an N·log(N) method for Ewald sums in large systems. *J. Chem. Phys.* **98**, 12 (1993).

73. Tian, Q. et al. Engineering of an endogenous hydrogen sulfide responsive smart agent for photoacoustic imaging-guided combination of photothermal therapy and chemotherapy for colon cancer. *J. Adv. Res.* **41**, 159 (2022).

74. Perez-Riverol, Y. et al. The PRIDE database resources in 2022: a hub for mass spectrometry-based proteomics evidences. *Nucleic Acids Res.* **7**, D543–D552 (2022).

Acknowledgements

Author contributions

F.Z.L., H.Y.Z., and J.G.P. designed research; K.Z., X.W.X., M.Y.C., T.X.Y., J.S., and B.L. performed research; K.Z., J.G.P. X.W.X. and L.J. analyzed data; F.Z.L., J.G.P., Y.H.W., H.S.Z., and L.J. supervised the experiments. K.Z., C.F.M., D.N.H., and L.J. wrote the paper. L.J. and J.G.P. provided critical insights and supervised the revision of manuscripts. All authors contributed to the final version of the manuscript.

Competing interests

The authors declare no conflict of interest.

Additional information

Supplementary information The online version contains supplementary material available at https://doi.org/10.1038/s41467-025-57376-7.

Correspondence and requests for materials should be addressed to Hongyue Zheng or Fanzhu Li.

Peer review information *Nature Communications* thanks Tyler Reddy, João B. Vicente, Adithya Polasa and the other, anonymous, reviewer(s) for their contribution to the peer review of this work. A peer review file is available.

Reprints and permissions information is available at http://www.nature.com/reprints

Publisher's note Springer Nature remains neutral with regard to jurisdictional claims in published maps and institutional affiliations.